Published in final edited form as:
Nat Med. 2019 August ; 25(8): 1310–1318. doi:10.1038/s41591-019-0531-2.

Multiscale reverse engineering of the human ocular surface

Jeongyun Seo[1], **Woo Y. Byun**[1], **Farid Alisafaei**[2], **Andrei Georgescu**[1], **Yoon-Suk Yi**[1], **Mina Massaro-Giordano**[3,4], **Vivek B. Shenoy**[2,5], **Vivian Lee**[3], **Vatinee Y. Bunya**[3,4], **Dongeun Huh**[1,5,6,*]

[1]Department of Bioengineering, University of Pennsylvania, Philadelphia, PA, USA

[2]Department of Materials Science and Engineering, University of Pennsylvania, Philadelphia, PA, USA

[3]Department of Ophthalmology, Scheie Eye Institute, Perelman School of Medicine, University of Pennsylvania, Philadelphia, PA, USA

[4]Penn Dry Eye and Ocular Surface Center, Perelman School of Medicine, University of Pennsylvania, Philadelphia, PA, USA

[5]NSF Science and Technology Center for Engineering Mechanobiology, University of Pennsylvania, Philadelphia, PA, USA

[6]Institute for Regenerative Medicine, Perelman School of Medicine, University of Pennsylvania, Philadelphia, PA, USA

Abstract

Here we present a miniaturized analog of a blinking human eye to reverse engineer the complexity of the interface between the ocular system and the external environment. Our model comprises human cells and provides unique capabilities to replicate multiscale structural organization, biological phenotypes and dynamically regulated environmental homeostasis of the human ocular surface. Using this biomimetic system, we discovered new biological effects of blink-induced mechanical forces. Furthermore, we developed a specialized in vitro model of evaporative dry-eye disease for high-content drug screening. This work advances our ability to emulate how human

---

Reprints and permissions information is available at www.nature.com/reprints.

[*]**Correspondence and requests for materials** should be addressed to D.H., huhd@seas.upenn.edu.

Author contributions
J.S. designed the research, performed the experiments and analyzed the data with assistance from W.Y.B., A.G. and Y.-S.Y., and wrote the manuscript. In collaboration with J.S. and D.H., F.A. and V.B.S. developed and analyzed a theoretical model of the engineered eye model. M.M.-G., V.L. and V.Y.B. conducted clinical studies of patients with DED and helped J.S. and D.H. collect and analyze tear osmolarity, keratography and fluorescein staining data. D.H. designed the research, analyzed the data and wrote the manuscript.

Competing interests
D.H. holds equity in Emulate Inc. and consults for the company.

Online content
Any methods, additional references, Nature Research reporting summaries, source data, statements of code and data availability and associated accession codes are available at https://doi.org/10.1038/s41591-019-0531-2.

Extended data is available for this paper at https://doi.org/10.1038/s41591-019-0531-2.

Supplementary information is available for this paper at https://doi.org/10.1038/s41591-019-0531-2.

Peer review information: Brett Benedetti was the primary editor on this article and managed its editorial process and peer review in collaboration with the rest of the editorial team.

physiological systems interface with the external world, and may contribute to the future development of novel screening platforms for biopharmaceutical and environmental applications.

Human organs possess complex multicellular structures that serve as structural and functional interfaces to the external environment[1–3]. To function as gatekeepers, these tissue assemblies have evolved multiscale architecture in which different types of specialized cells are organized in a hierarchical manner to form three-dimensional (3D) barrier structures. They are also equipped with dynamically regulated homeostatic mechanisms to maintain their stability in the face of a constantly changing environment[1–5]. Despite advances in our understanding of these living interfaces, emulating their complex features in an integrated and human-relevant context remains a major challenge.

Here we describe a multiscale reverse-engineering strategy to tackle this challenge using the ocular surface of the human eye as a model system. We show that human corneal and conjunctival cells can be combined with a synthetically created yet physiological culture environment to replicate the key biological features of the ocular surface at the cellular, tissue and whole organ levels. Integrated with a digitally controlled instrumentation platform, our model also makes it possible to mimic spontaneous eye blinking and to study the biological effects of blink-induced mechanical forces. To demonstrate the practical applications of this system, we present an in vitro model of dry-eye disease (DED) that can be used as a screening platform to assess the therapeutic efficacy of investigational drugs.

Results

Model design and construction

The ocular surface is an organscale structure that forms the dome-shaped outermost layer of the eye. At the tissue level, the ocular surface consists of the cornea and conjunctiva (Fig. 1a), each of which represents a multilayered barrier structure. The cornea is lined with a stratified epithelium and supported by subepithelial stroma interspersed with keratocytes (Fig. 1b). At the margin of the cornea, the epithelium grades into the conjunctiva composed of a goblet cell-containing stratified epithelium and the underlying connective tissue (Fig. 1b). Another important feature of the ocular surface is spontaneous blinking, during which transient closure and subsequent reopening of the eyelids spread secreted tears over the ocular surface to form a lubricating tear film that provides a smooth refractive surface (Fig. 1c).

To mimic these essential features, we have developed an in vitro model of the human ocular surface (Fig. 1d). This system is created in a multilayered device consisting of a dome-shaped 3D cell culture scaffold (Fig. 1e,f and Supplementary methods) bonded to an underlying perfusion chamber, a tear channel and a biomimetic eyelid that can be actuated to slide back and forth on the scaffold surface (Fig. 1g and Supplementary Videos 1 and 2). To mimic the subepithelial stroma, primary human keratocytes are embedded in an extracellular matrix hydrogel in the scaffold (Fig. 1h and Supplementary methods). Subsequently, the concentric pattern of the corneal and conjunctival epithelia is reproduced (Fig. 1i) using a 3D cell patterning technique (Extended Data Fig. 1).

Recapitulating physiological phenotypes of the human ocular surface

For production of physiological ocular surface tissue in our model, the seeded epithelial cells were first grown to confluence in submerged conditions and then cultured at the air-liquid interface (ALI) to recapitulate their native organ-specific environment. Prolonged (>2 weeks) ALI culture led to substantial morphological and biochemical changes indicative of cell differentiation. First, the corneal cells formed a stratified epithelium consisting of seven to eight stacked cell layers supported by an underlying keratocyte-laden matrix that resembled the corneal epithelium in vivo[6] (Fig. 2a). The epithelium also showed a layer of cells that expressed a basal cell-specific marker (p63) (Fig. 2b). In addition, the differentiated cells formed tight junctions (Fig. 2c) and microscopic protrusions on their apical surface that were identical to microvilli and microplicae on the human cornea[7] (Fig. 2d). These morphological changes were accompanied by substantially increased expression of cytokeratin-3 and −12 (CK-3/12) (Fig. 2e), which are specific to terminally differentiated corneal epithelial cells. Importantly, the increase in CK-3/12 expression during ALI culture was significantly greater than that measured in submerged culture (Fig. 2e).

ALI culture also induced the stratification of the conjunctival epithelium (Fig. 2f) and the expression of differentiation markers such as cytokeratin-19 (CK-19) (Fig. 2g) and mucin protein (MUC16) (Fig. 2h). The secretory function of the engineered ocular surface was demonstrated by significantly increased mucus production due to ALI culture (Fig. 2i). Interestingly, scanning electron microscopy revealed interconnected networks of ultrafine filamentous structures along the outer tips of the microvilli (Fig. 2j), closely resembling the glycocalyx on the human ocular surface that plays a critical role in the stabilization of the tear film and protection against foreign insults[8,9].

Emulating spontaneous eye blinking and physiological tear film dynamics

Next, we set out to reproduce eye blinking and its function as a regulator of tear film dynamics, a critical feature of the ocular surface not properly modeled in previous in vitro studies[10–12]. To this end, we incorporated a biomimetic analog of eyelids made out of biocompatible hydrogel (Fig. 3a and Supplementary methods). The motion of the eyelid was controlled by an electromechanical actuator (Supplementary methods) to generate cyclic back-and-forth movements at 0.2 Hz following the kinematics of spontaneous blinking in the normal human eye[13] (Fig. 3b). Tear production and secretion from the lacrimal glands were simulated by controlled outflow of contrived tears through small orifices in the tear channel (Fig. 3c) at physiological rates of tear secretion in the human eye[14]. The secreted fluid was then pushed by the eyelid during its downward movement and spread over the scaffold to form a liquid film, which was visible at the completion of the reopening phase (Fig. 3d). This actuation also resulted in the flow of excess tears into the drainage channel (Fig. 3e). Optical coherence tomography (OCT) revealed a very thin fluid layer on the epithelial surface (Fig. 3f) with an average thickness of 6 μm, closely approximating physiological tear film thickness in the human eye (5–10 μm)[15].

Computational analysis of blink-induced biomechanical forces

The motion of the eyelid during blinking produces different types of mechanical forces on the ocular surface that together give rise to complex stress fields[16,17]. To investigate this biomechanical environment, we developed a theoretical elasto-hydrodynamic model for quantitative analysis of mechanical stresses and structural deformation of the engineered ocular surface due to blinking (Fig. 3g and Supplementary methods).

This study revealed large pressure gradients in the tear meniscus along the edge of the eyelid (Fig. 3h). A maximum pressure was estimated to be 1.9 kPa, which fell within the physiological range (0.3–7 kPa) of upper eyelid pressure on the ocular surface measured in the human eye[18–21]. Additionally, spatial mapping of pressure showed a narrow region of positive pressure and minimum tear film thickness resulting from the close proximity of the eyelid margin to the ocular surface (Fig. 3h and Supplementary methods). The width of this area (proximity width) was approximately 0.85 mm, which was in excellent agreement with the average width (0.6 mm) of the primary contact region in the human eye[20,21].

Similar to pressure, fluid shear stress showed large fluctuations in the proximity region (Fig. 3i). Outside this area, stress was reduced to substantially lower yet still significant levels. Although clinical data do not exist for direct comparison, our prediction is comparable to the levels of shear stress reported in previous studies of blink-induced tear flow[17,22]. Our analysis also revealed shallow depressions around the center of the ocular surface (Fig. 3j). Interestingly, the width of this region (1.5 mm) closely approximated the clinically measured average width (1.3 mm) of corneal surface deformation due to upper eyelid pressure in the human eye[20,21].

Identification of mechanosensitive responses to eye blinking

Motivated by our limited understanding of the biological effects of blink-induced mechanical forces[17,23,24], we then examined responses of the engineered ocular surface to blinking with a specific focus on the differentiation of corneal epithelial cells. As part of this study, we first confirmed that the repetitive eyelid movement did not induce any detrimental effects on the corneal epithelial cells (Fig. 3k). This mechanical stimulation, however, significantly enhanced their differentiation. In comparison to those maintained at ALI alone (Fig. 3l; top left), the epithelial cells subjected to a combination of ALI and blinking for 24 h (Fig. 3l; bottom left) showed a more than fourfold increase in CK-3/12. The marker expression was further upregulated after 48 h blinking (Fig. 3l; bottom right), reaching a level that was approximately nine times higher than that in the ALI group (Fig. 3l).

Engineering a pathophysiological model of DED

Next, we investigated the feasibility of further engineering our system to model DED. DED is caused by disrupted homeostatic balance of the tear system that results in instability of the tear film and increased tear osmolarity (hyperosmolarity)[10,25–27], which together lead to injurious epithelial stress and a self-perpetuating cycle of inflammation[10,28,29]. In a large fraction of patients with DED, these pathological changes are driven by evaporation-induced excessive water loss from the ocular surface[10,30] (Fig. 4a). To mimic this evaporative type of DED, we first constructed a digitally controlled simulation platform to maintain the engineered ocular surface under conditions that approximated the local atmospheric environment (Supplementary methods and Supplementary Video 3). In this system, DED was induced by decreasing the frequency of blinking actuation to six times per minute to simulate reduced blinking rates in patients with DED[30].

To characterize this model, we examined evaporative water loss from the tear film by applying an absorptive paper strip (Schirmer strip) to the base of the scaffold and measuring the length of wetting to quantify the volume of tear fluid (Fig. 4b). In comparison to the devices maintained at physiological blinking rates (12 times per minute), our DED model showed significantly decreased wetting, indicating reduced tear volumes (Fig. 4b). Given that the rate of tear secretion was the same in these groups, this reduction can be attributed to increased tear evaporation due to the prolonged interblink period.

We then investigated whether our disease model was capable of reproducing the hyperosmolarity and instability of the tear film in patients with DED, which are the core mechanisms of DED[10,28]. We first evaluated tear osmolarity using the TearLab Osmolarity System (Supplementary methods). Compared with an average tear osmolarity of 307 mOsm l^{-1} in the control model with physiological blinking conditions, tears sampled from our disease model showed significantly higher osmolarity (351 mOsm l^{-1}) (Fig. 4c). Importantly, clinical data generated from the same analysis of normal subjects and patients with DED were in good correlation with our in vitro results (Fig. 4c).

To investigate the instability of the tear film, we used a clinical imaging instrument (OCULUS Keratograph 5M) that can generate illuminated patterns of concentric rings on the ocular surface and monitor their stability for detection of tear film break-up (Fig. 4d and Supplementary methods). A single blink in our device produced ring patterns on the surface of the engineered tissue that resembled those observed on the human ocular surface (Fig. 4d). These patterns remained relatively stable for extended periods (10 s) in normal conditions (Fig. 4e; first quadrant). In contrast, the rings generated in the DED model became irregular and unstable more rapidly (Fig. 4e; fourth quadrant). Quantitative spatial mapping of tear film break-up (Supplementary methods) confirmed these findings and revealed significantly more rapid break-up of the tear film over a larger surface area in the DED model (Fig. 4f). The average tear film break-up times estimated in the normal (10.18 s) and DED (5.53 s) devices approximated those measured in healthy human subjects (10.31 s) and patients with DED (7.49 s)[31–33].

Investigation of biological responses in the dry-eye model

Our study also examined the deleterious potential of dry-eye conditions to induce epithelial damage and pro-inflammatory responses, which represent the key pathological features of DED[10,28,29]. We first assessed ocular surface injury using a traditional diagnostic technique that relies on the localization of sodium fluorescein dye in areas of cellular degeneration or death[34]. The control group representing a healthy ocular surface exhibited no detectable fluorescence (Fig. 4g; third quadrant), which was in agreement with the staining data from healthy human subjects (Fig. 4g; second quadrant). In the DED model, however, a large portion of the epithelial surface showed strong and persistent staining (Fig. 4g; fourth quadrant) in a manner similar to that observed in human patients (Fig. 4g; first quadrant). Presumably, this difference was caused by increased fluorescein absorption into intercellular spaces and subepithelial stroma in the DED model due to desiccation-induced epithelial injury and disruption of intercellular junctions[34]. Of note, the same experiment conducted in a Transwell-based dry-eye model[11] resulted in no fluorescein staining of the tissue (Extended Data Fig. 2).

We then investigated whether the hyperosmolarity of the tear film in the DED model can activate corneal and conjunctival epithelial cells to produce inflammatory cytokines, chemokines and matrix enzymes implicated in the progression of DED[10,28]. We selected interleukin (IL)-8, IL-1β, tumor necrosis factor (TNF)-α and matrix metalloproteinase (MMP)-9 as representative inflammatory mediators and measured their levels in tear samples during the early induction of DED. As shown in Fig. 4h, reduced blinking in the DED model noticeably increased cytokine concentrations within the first 2 d. Increased release of the same cytokines was also observed in the control group maintained at the normal blinking rate (12 times per minute) (Fig. 4h). This response, however, was followed by rapid reduction of cytokines to the baseline levels measured before the initiation of dynamic culture (day 0 in Fig. 4h). This result suggests that the environmental changes due to blinking and altered humidity required for setting up our experiments may elicit transient inflammatory responses even in the normal control group. Our DED model exhibited a similar behavior initially but the levels of cytokines remained elevated over the entire duration of culture, indicating non-resolving inflammation. Our analysis also showed similar temporal profiles of MMP-9 production.

Evaluation of the therapeutic potential of lubricin

In the next phase of our study, we explored the potential of our DED model as a preclinical drug screening platform. This study focused on testing the efficacy of lubricin, a mucin-like glycoprotein first identified in the synovial joint as a natural boundary lubricant[35,36]. In the eye, lubricin is produced by corneal and conjunctival epithelial cells and binds to the epithelium to form brush-like structures that lower friction between the ocular surface and the eyelid[37,38] (Fig. 5a). Studies have suggested that this natural lubrication mechanism may be impaired in DED due to reduced biosynthesis or loss of lubricin[39,40]. This also led to a recent clinical trial of recombinant human lubricin that showed rapid (<2 weeks) and significant improvements of clinical signs and symptoms of DED[40].

In our DED model, the ocular surface clearly showed the deficiency of endogenous lubricin (Fig. 5b; DED) compared with the normal control group (Fig. 5b; Normal), corroborating the previously suggested association of dry eye with reduced lubricin[39,40]. When topically treated with a lubricin formulation, however, the corneal epithelium was replenished with exogenous lubricin, which remained adherent on the surface during blinking (Fig. 5b; +Lubricin). Importantly, the applied lubricin lubricated the ocular surface against a sliding hydrogel eyelid more effectively than did saline and pure contrived tears, as evidenced by significantly decreased static and kinetic friction coefficients (Fig. 5c). This friction-lowering effect was observed consistently at different sliding velocities tested in our experiments, supporting the therapeutic potential of exogenous lubricin as a functional substitute for endogenous boundary lubricants[40].

While the friction coefficient provides a useful quantitative measure of lubrication, clinical evaluation of ophthalmic lubricants requires the analysis of patient outcome variables indicating the health of the ocular surface[40], which is not currently possible in preclinical studies. Therefore, we leveraged the compatibility of our model with standard methods of clinical investigation to examine how lubricin affected two representative outcome variables. First, keratography revealed that treatment of the desiccated ocular surface with a clinically relevant dose of lubricin noticeably delayed the postblink destabilization of the tear film (Fig. 5d), as verified by significantly increased tear break-up time and the reduced area of tear film rupture (Fig. 5e,f). The quantitative measurements from the drug-treated devices were comparable to those from the normal group without DED symptoms. Lubricin also changed fluorescein staining of the ocular surface, which is another important clinical outcome measure. After 3 d drug treatment, the ocular surface in the DED model appeared intact and was resistant to fluorescein staining (Fig. 5g), resembling the healthy ocular surface model (Fig. 4g). Importantly, these beneficial effects of lubricin are similar to the improvements of corneal fluorescein staining and tear break-up times reported in the recent clinical trial of recombinant human lubricin[40].

Discovery of therapeutic effects of lubricin

Finally, we used our DED model to investigate the added therapeutic value of lubricin beyond its capacity as a lubricant. Given the central role of inflammation in dry eye[10,28,29], we asked whether topically administered lubricin could modulate inflammatory signaling pathways in the ocular surface.

Our analysis first focused on toll-like receptor-4 (TLR-4) in the corneal epithelial cells, which was significantly upregulated by the desiccation of the ocular surface in the DED model as compared with control[41] (Fig. 5h; Normal versus DED). Interestingly, epithelial treatment with lubricin changed this pro-inflammatory phenotype by downregulating the expression of TLR-4 (Fig. 5h; +Lubricin). The immunomodulatory capacity of lubricin was further evidenced by its effect on nuclear factor (NF)-κB, which is a downstream mediator of TLR signaling[42]. Excessive tear evaporation in the DED model activated NF-κB as illustrated by its nuclear translocation in the corneal epithelial cells (Fig. 5i; Normal versus DED). When treated with lubricin, however, the vast majority of cells showed the redistribution of NF-κB to the cytoplasm (Fig. 5i; +Lubricin).

For further verification, we examined the effect of lubricin on the tear levels of IL-8, TNF-α, IL-1β and MMP-9. In the DED model, the baseline measurement in the absence of lubricin clearly showed substantially elevated cytokine and enzyme levels throughout the culture period (Fig. 5j; triangle versus circle). When lubricin was administered after 4 d culture in dry-eye conditions, however, our disease model showed a marked decline in all of the analytes (Fig. 5j; square). In these devices, the concentrations of the mediators remained low for the entire duration of treatment and statistically indistinguishable from those in the normal group.

Discussion

Our blinking eye model represents an advanced in vitro technology that offers new strategies to mimic and interrogate the critical living interface between the human eye and the external world. By combining an engineered synthetic environment with living human cells, this hybrid system makes it possible to emulate the multiscale features and dynamic behavior of the human ocular surface. The capabilities demonstrated in this study make our eye model an attractive platform to address previously inaccessible questions and important unmet needs.

For example, the ability to mimic blinking provides opportunities to investigate the mechanobiology of the human ocular surface. Despite early studies suggesting that blinking may increase the shedding of the corneal epithelium and affect epithelial cell migration[23,24], it has been technically challenging to examine this important aspect of ocular surface physiology at the cellular and tissue levels due to the limitations of existing experimental model systems. Thanks to the blinking capabilities of our model, this study shows that blink-induced physiological mechanical forces may have significant contributions to the differentiation of human corneal epithelial cells. While further studies are needed to understand the underlying mechanisms, this mechanosensitive response as shown by the increased expression of cytokeratins, which are the key component of intermediate filaments, may be interpreted as a protective mechanism that allows corneal epithelial cells to form more robust cytoskeletal structures to withstand externally applied forces during blinking. Considering that blinking produces different types of mechanical forces, however, the relative contributions of these forces to the observed response remain to be elucidated. Nevertheless, these results suggest that our model may serve as a potentially powerful platform to examine whether and how physiologically relevant biophysical cues affect cellular phenotype and function in the human ocular surface.

The drug testing study using lubricin also provides a great example of opportunities enabled by our technology. Based on recent evidence that altered mechanical interactions between the blinking eyelid and the ocular surface play a critical role in the pathophysiology of DED[37,38,40,43,44], there is rapidly growing interest in developing new drugs that target the pathophysiological biomechanical environment of dry eye[10,45]. Investigating this promising therapeutic approach, however, remains a challenge due to the limitations of current in vitro platforms that largely fail to capture the dynamic environmental features of the ocular surface[45,46]. While laboratory animals provide alternatives, the well-documented interspecies differences in the dynamics of blinking and the tear film make this strategy problematic[10,46,47]. As evidenced by the failure of several recent clinical trials of dry-eye therapies validated by preclinical mouse studies[45], animal models also face increased scrutiny regarding their capacity to simulate the underlying pathophysiology of human DED[10,45,46,48].

Using lubricin as a model investigational drug, our study suggests that these limitations may be addressed by exploiting our blinking eye model as a human-relevant preclinical platform to recapitulate biomechanical disease processes of DED. This advanced capability of our DED model allowed us to test and validate the efficacy of lubricin as an ophthalmic lubricant. Moreover, our study discovered previously unknown therapeutic effects of lubricin on ocular surface inflammation. The molecular mechanism of this finding remains to be elucidated but, based on recent reports that lubricin can bind to pattern-recognition receptors and regulate their immunomodulatory activity[49,50], we speculate that the anti-inflammatory effects may be mediated in part by the inhibitory interaction of exogeneous lubricin with

TLRs on the cornea. Since abnormally altered mechanical forces can trigger inflammatory responses[37,43,44], enhanced surface lubrication due to lubricin may be another contributor to reduced inflammation. It should be noted that lubricin has recently been suggested as an important regulator of immunity during the homeostasis of articular cartilage and the pathogenesis of post-traumatic or degenerative joint diseases[35,49–51]. This study shows the therapeutic anti-inflammatory potential of lubricin in the setting of DED. These results collectively suggest that exogenous human lubricin may offer multifaceted therapeutic benefits by acting on both biomechanical and biochemical disease processes.

Finally, our work provides a rare example of translating cell culture into clinical settings to create a platform that can be interfaced with human-scale diagnostic tools and standard methods of clinical investigation. As demonstrated in our DED and lubricin studies, this unique capability made it possible to generate in vitro data directly comparable to clinical findings, greatly facilitating the process of validating the physiological and clinical relevance of the model. These types of systems may be instrumental to the assessment of in vitro–in vivo correlation and eventually contribute to rapid translation of research discoveries into clinical tests and therapies.

Since our reverse engineering approach involves simplification of in vivo characteristics using minimal design features, our model still shows significant differences from its in vivo counterpart. For example, our system fails to reconstitute the vascularity and the immune cell components in the conjunctiva, which is particularly important for modeling immune responses in complex ocular diseases such as dry eye[10]. Inclusion of corneal nerve cells may also render our model more representative of the native system considering their essential role in controlling eye blinking and maintaining healthy ocular surface tissue[52,53]. The demonstrated method of using external pressure to secrete contrived tears from a microfabricated channel is also significantly divergent from the process of tear production and secretion from the lacrimal and meibomian glands in the native eye[54]. Finally, our system as a stand-alone organ model is inherently limited in its ability to simulate systemic interactions of the ocular surface with other physiological systems, for which animal models provide a more viable approach.

Despite these limitations, our technology still represents a significant breakthrough for in vitro modeling of the human eye. For practical applications, our system holds great potential as a drug screening platform for high-content and multiscale analysis of human ocular responses to ophthalmic drugs. The application of our technology can also be readily extended to in vitro evaluation of consumer products, environmental materials, surgical procedures and indwelling biomedical devices (for example, contact lenses). While much remains to be accomplished, we believe that our work embodies major conceptual and technical innovations that represent important first steps towards the ultimate goal of reverse engineering the complex interaction of the human body with the external environment.

Methods

Primary cell culture

Primary human corneal epithelial cells (CellnTec) were maintained in CnT-Prime medium (CellnTec) supplemented with 1% penicillin and streptomycin (P/S) according to the manufacturer's protocols. Immortalized human conjunctival epithelial cells were a gift from Dr. Ilene Gipson at the Schepens Eye Research Institute of Massachusetts Eye and Ear. These cells were grown in keratinocyte serum-free medium (Gibco) supplemented with bovine pituitary extract (0.05 mg ml^{-1}), human recombinant epidermal growth factor (0.2 ng ml^{-1}), $CaCl_2$ (0.4 mM) and 1% P/S. Primary human keratocytes were obtained from ScienCell and cultured in fibroblast medium (ScienCell) supplemented with 2% fetal bovine serum, fibroblast growth supplement and 1% P/S. The cells were maintained at 37 °C in a humidified incubator with 5% CO_2 in air and used at low passage numbers (<4).

Culture of engineered ocular surface

After cell seeding, the inlet of the perfusion chamber was connected to a programmable syringe pump to generate a continuous flow of culture medium on the basal side of the scaffold at a volumetric flow rate of 100 μl h^{-1} using a programmable syringe pump (Braintree Scientific). The apical side of the epithelial cells was submerged in medium for 2 d to allow for cell proliferation. During this culture period, the entire experimental setup was kept in a humidified cell culture incubator maintained at 37 °C and 5% CO_2. Once a confluent monolayer was formed, medium was gently aspirated from the open well to expose the epithelial cells to an ALI. The engineered ocular surface tissue was then maintained at an ALI for 14 d in a humidified cell culture incubator. During ALI culture, the cells were sustained by a steady flow of medium through the perfusion chamber at a rate of 100 μl h^{-1}.

Histology and hematoxylin and eosin (H&E) staining of ocular surface tissue

For histological analysis of differentiated corneal and conjunctival tissue, the cell culture scaffold was gently washed by flushing the perfusion chamber and the open well with PBS. Following fixation of the engineered tissue by 4% paraformaldehyde (PFA) in PBS overnight at 4 °C, the scaffold was then rinsed with PBS, removed from the polydimethylsiloxame (PDMS) device using a scalpel and transferred into a 6-well plate for further processing. For tissue dehydration, the scaffold was submerged and equilibrated in 30%, 50%, 70%, 80%, 90%, 95% and 100% ethanol in a sequential manner. After dehydration, the scaffold was incubated with a clearing agent for 30 min and transferred to a 50:50 mixture solution of clearing agent and molten paraffin wax for incubation at 65 °C for 30 min, followed by incubation in 100% molten wax for another 60 min. After embedding, the scaffold was sectioned into 10-μm slices.

For H&E staining, the paraffin-embedded sections were deparaffinized first in a clearing agent (CitriSolv, Fisher Scientific) and gradually rehydrated in 100%, 95%, 70% and 50% ethanol. After rinsing in distilled water for 1 min, the sections were stained with hematoxylin (hematoxylin solution, Sigma Aldrich) for 1 min and then washed with tap water for 3 min. This step was followed by treatment of the sections with bluing reagent

(Scott's buffer) for 20 s, rinsing in tap water for 3 min and staining with eosin (eosin Y alcoholic, Sigma Aldrich) for 20 s. Finally, the slides were rinsed with 95% ethanol twice for 1 min each, 100% ethanol for 1 min and the clearing agent for 1 min. The final slides were mounted (Permount, Fisher Scientific) and sealed with a coverslip.

Immunostaining of epithelial cells

The engineered ocular surface tissue was first washed with PBS and fixed with 4% PFA for 15 min. The cells were then permeabilized with 0.25% Triton X-100 for 5 min, treated with a blocking buffer (1% BSA in PBS) for 1 h at room temperature and incubated in a primary antibody solution overnight at 4 °C, followed by staining of secondary antibodies for 1 h. Nuclear staining was also performed using 1 μg ml^{-1} DAPI (Invitrogen) for 5 min. The scaffold was then cut out from the PDMS device and placed between coverslips using a fluorescent mounting medium (DAKO). The cells were not permeabilized for TLR-4 staining. Information about the primary and secondary antibodies used in our studies is provided in the Supplementary information.

Scanning electron microscopy imaging of engineered ocular surface

For scanning electron microscopy, the ocular surface tissue was cultured for a total of 16 d (3 d submerged culture followed by another 13 d ALI culture). On day 16, the scaffolds were washed with PBS, carefully removed from the PDMS device and stored in 2.5% glutaraldehyde fixative in 0.1 M phosphate buffer at room temperature until further processing. After fixation, the samples were rinsed in 0.1 M phosphate and postfixed in 1% buffered osmium tetroxide for 90 min at 4 °C. The sequential dehydration steps were then performed in 30%, 50%, 75%, 95% and 100% ethanol for 10 min. Subsequently, the scaffolds were completely dried using a critical point dryer and coated with gold.

Alcian blue-periodic acid Schiff (AB-PAS) staining

To visualize mucin production by the ocular surface tissue in our model, AB-PAS staining (DAKO) was performed. For the day 2 group, the engineered tissue was fixed with 4% PFA after 2 d culture. The devices in day 16 groups were cultured submerged for 2 d and then maintained submerged or at an ALI for 14 d before fixation. Acellular devices were used to represent a negative control group. For staining, the engineered tissue was first stained with alcian blue for 30 min and washed thoroughly with deionized water. The samples were then treated with periodic acid for 5 min, rinsed in deionized water, incubated with the Schiff's reagent for 15 min and washed in lukewarm running tap water for 10 min. The staining procedure was completed with a final washing step using deionized water. Mucin expression was quantified by measuring the intensity of AB-PAS staining in the photos of the entire ocular surface taken by a digital camera (Nikon).

Preparation of contrived tear solution

Lipid-containing contrived tears were prepared according to the manufacturer's protocols (Contrived Tears with Lipids, Ursa BioScience). Briefly, the vials of aqueous tears and concentrated lipid components were equilibrated at room temperature for 30 min and then briefly sonicated for 10 min to remove any precipitates in the solutions. To reconstitute complete tears with lipids, 10 μl of the stock lipid solution was mixed with 4.5 ml of the aqueous tears in a vial, which was then left open for 30 min in a sterile biosafety cabinet to evaporate the lipid phase transfer solution. The composite tears were then sonicated for 10 min and left in a biosafety cabinet for an additional 10 min. During experiments, contrived tears were injected into the tear channel using a programmable syringe pump (Braintree Scientific) at 100 μl h^{-1}.

Preparation of gelatin-based hydrogel

The biomimetic eyelid incorporated into the engineered ocular surface model was made out of gelatin methacryloyl (gel-MA) which offered mechanical flexibility, structural stability and ease of fabrication. To synthesize gel-MA, 10 g of type A porcine skin gelatin (Sigma Aldrich) was dissolved into 100 ml PBS (10% w/v) in a glass beaker and incubated at 65 °C. Once gelatin was fully dissolved, methacrylic anhydride was added dropwise to the gelatin solution at 100 μl h^{-1} (140 μl methacrylic anhydride per gram of gelatin) and allowed to react for 4 h while being covered with aluminum foil. Following the reaction step, 400 ml of prewarmed (65 °C) PBS was poured into the mixture of gelatin and methacrylic anhydride at a dilution ratio of 5:1 to stop the reaction. The solution was then transferred into a dialysis bag having a filter membrane with a cutoff size of 12–14 kDa. This bag was placed and kept in a bucket of deionized water at 50 °C for 3 d, over which time dialysis was performed to remove unreacted methacrylic anhydride and salts. During this process, deionized water was changed twice a day. After 3 d dialysis, the gel-MA solution was aliquoted into 50-ml conical tubes and stored at −80 °C overnight until completely frozen. The solution was then lyophilized for 4 d and stored at −20 °C until use.

Fluorescein staining

After rinsing the engineered ocular surface with PBS, a sterile fluorescein sodium ophthalmic strip (Ful-Glo, Akorn) was laid at the base of the scaffold. The eyelid was then actuated to blink a few times, during which fluorescein was released from the strip and taken up by contrived tear fluid spreading on the ocular surface. Afterwards, the engineered tissue was illuminated with cobalt blue light and photographed for further analysis.

Collection of tear samples

During the induction of dry eye in our device, tears were collected for analysis of cytokines and matrix enzymes. Tear fluid was sampled at the margin of the eyelid using 3-μl glass microcapillary tubes (Microcaps, Drummond Scientific). Each tube was then placed in a precooled Eppendorf tube and preserved in a −80 °C freezer until analysis.

OCT imaging of tear film

An optical coherence tomography (OCT) system (Envisu R2200, Leica) developed for ophthalmology research was used to visualize the tear film on the epithelial surface of our model. During imaging, the engineered ocular surface was vertically oriented and mounted on the OCT system using a custom-designed device holder. The engineered eye model blinking at 0.2 Hz was then scanned along the center of the scaffold using a 12-mm high-resolution telecentric lens designed for imaging the anterior segment of the eye.

Analysis of cytokines and MMP-9

The concentration of inflammatory mediators in the collected tear samples was measured using multiplexed cytokine kits for IL-1β, IL-8, TNF-α and MMP-9 (Milliplex MAP human high-sensitivity cytokine and MMP magnetic bead panels, Millipore) according to the procedure provided by the manufacturer.

Measurement of friction coefficients

The coefficient of friction between the engineered ocular surface and the hydrogel eyelid was measured using previously reported methods[37,38,55]. Briefly, the ocular surface tissue cultured under DED conditions for 4 d was rinsed with PBS twice and fixed in 4% PFA for 15 min. The scaffold was then removed from the PDMS device using a biopsy punch (diameter = 6 mm), placed on top of a dome-shaped pedestal made of PDMS and glued along the circular base using epoxy. After curing, the resultant structure was attached to the rotational stage of a Bose ELF3200. Separately, an annulus of gel-MA (outer radius: $r_o = 3$ mm; inner radius: $r_i = 1$ mm) was prepared on a thin PDMS substrate for mechanical testing, which was fixed to the linear actuator of the Bose ELF3200 system. Following sample mounting, the ocular surface tissue received 100 μl test lubricant and was brought in contact with the gel-MA annulus.

Mechanical testing was performed following previously reported methods[55]. During testing, the sample was axially loaded with approximately 0.4 ± 0.1 N and rotated at 2 effective sliding velocities v_{eff} (1 and 10 mm s^{-1}), where $v_{\text{eff}} = \omega \times r_{\text{eff}}$ and $r_{\text{eff}} = 2/3\left[\left(r_o^3 - r_i^3\right)/\left(r_o^2 - r_i^2\right)\right]$. Axial load and torque data were collected at 50 Hz. To quantitatively evaluate the friction-lowering effect of tested solutions, static and kinetic friction coefficients (μ) were calculated using an equation $\mu = \tau/(r_{\text{eff}} \times N)$, where τ and N represent torque and normal load, respectively. The analysis of static friction coefficient was conducted using a maximum torque that occurred within the first 10° of rotation, whereas an average torques during rotation was used to calculate the kinetic friction coefficient. The results were normalized with respect to the friction coefficients obtained from the saline group at $v_{\text{eff}} = 1$ mm s^{-1}.

Preparation and administration of lubricin

Human lubricin was purified from conditioned media collected from confluent human synovial fibroblasts using the methods previously described[56]. In each device, topical administration of lubricin was accomplished by dispensing a single drop of lubricin onto the epithelial surface twice a day (in the morning and evening) over a period of 3 d.

Clinical evaluation of patients with DED and controls

Patient selection—The study was approved by the Institutional Review Board at the University of Pennsylvania, was HIPAA (The Health Insurance Portability and Accountability Act) compliant and adhered to the tenets of the Declaration of Helsinki. Subjects who were 18 years of age or older were recruited from the ophthalmology and rheumatology practices at an academic center. Informed consent was obtained from all participants before participation. Evaporative dry-eye subjects were enrolled if they had a history of blepharitis and had clinical signs of at least moderate blepharitis. Controls were enrolled if they did not have significant dry-eye symptoms (as indicated by an Ocular Surface Disease Index[57] score of less than 13) and had no previous or current diagnosis of DED or blepharitis.

Exclusion criteria for all subjects included a history of any significant ocular surface disease (other than DED) or ocular inflammation, thyroid eye disease, diabetes, active ocular infection, active ocular allergy, ocular surgery within 1 year, punctal plug placement within 30 d, evidence of lid deformity or abnormal lid movement disorder, use of eye drops (excluding artificial tears), contact lens use within 1 month, pregnancy or lactation, birth control or hormone replacement therapy, abnormal nasolacrimal drainage, evidence of a systemic disease known to affect tear production or the use of artificial tears within 2 h of enrollment. Subjects were also excluded if they had initiated or altered the dose of chronic systemic medication known to affect tear production within 30 d of testing. For all subjects, demographic information and medical and ocular history were obtained. Subjective symptoms of dry eye were assessed using the Ocular Surface Discomfort Index (Allergan). All subjects also underwent tear osmolarity testing, a slit lamp exam and vital dye staining with fluorescein.

Tear osmolarity—Tear osmolarity was measured in each eye with TearLab (TearLab Osmolarity System, TearLab Corp.). A 50-nl tear sample was collected atraumatically from the inferior lateral tear meniscus of each eye, always starting with the right eye. To ensure proper functioning of the instrument, the system calibration was validated at the start of each day of testing in accordance with the manufacturer's instructions. Due to the possible variability of measurements in patients with DED as previously described[27], three consecutive osmolarity measurements were taken at 1-min intervals in each eye of each subject using the same pen, always starting with the right eye. Three measurements per eye were taken at each of three sessions throughout the day (09:00 to 10:00, 12:00 to 13:00, 15:00 to 16:00) by the same examiner.

Corneal fluorescein staining—After tear osmolarity testing, 1 drop of sterile saline was used to wet a 1-mg fluorescein dye strip (Bioglo, Accutome), which was then applied to the inferior conjunctival fornix of both eyes. The patient was then asked to blink a few times to distribute the dye over the ocular surface. After 1–2 min, the cornea was then examined with the slit lamp at ×10 magnification using the cobalt blue light source. Fluorescein staining of the cornea was graded using the van Bijsterveld scale[58].

Statistical analysis

All results were reported as mean ± s.e.m. Statistical differences were analyzed using an unpaired, two-sided *t*-test except for analysis of inflammatory mediators in Figs. 4h and 5j. In Fig. 4h, we used a two-way analysis of variance (ANOVA) to compare two independent variables and multiple *t*-tests using the Holm–Sidak method to determine statistical significance between the two groups for each time point. A two-way ANOVA followed by Tukey's multiple comparisons test was used for statistical analysis in Fig. 5j. The number of times experiments were repeated and P values are reported in the figure legends and source data.

Reporting Summary

Further information on research design is available in the Nature Research Reporting Summary linked to this article.

Data availability

The data sets that support the findings of this study are available from the corresponding author upon reasonable request. All requests for raw and analyzed data and materials are promptly reviewed by the University of Pennsylvania to verify whether the request is subject to any intellectual property or confidentiality obligations. Any data and materials that can be shared will be released via a Material Transfer Agreement.

Extended Data

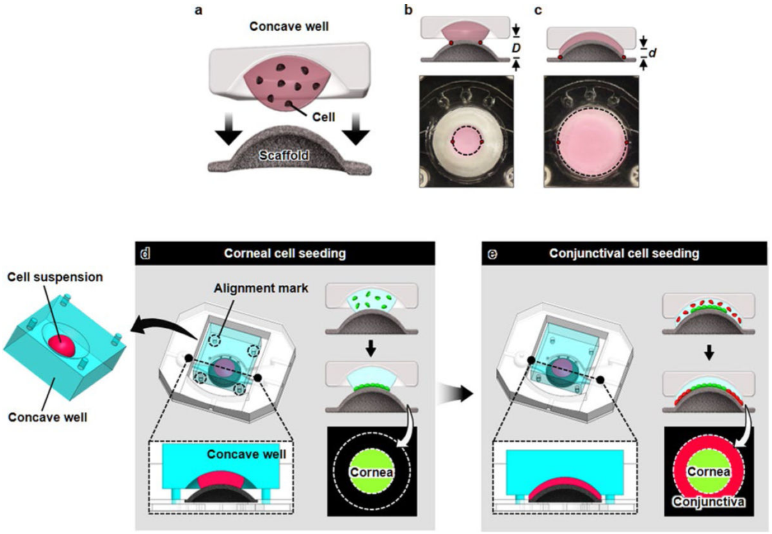

Extended Data Fig. 1 |. Formation of corneal and conjunctival epithelia using 3D cell patterning technique.

The concentric pattern of the ocular surface epithelia was replicated by plating human corneal and conjunctival epithelial cells on the surface of the scaffold following the formation of keratocyte-laden stroma. **a**, A 3D cell patterning technique is enabled by precisely controlled spreading of a cell suspension solution on the dome-shaped scaffold depending on the distance between a concave well and the convex surface of the scaffold. **b**, At a large distance (D), a cell-suspension solution sandwiched between the concave well and the convex scaffold forms a liquid bridge that wets the center of the scaffold and its vicinity. The meniscus of the solution is marked with a dotted line in the figure. **c**, When the well is brought in closer proximity to the scaffold ($d \ll D$), the liquid bridge spreads outward in the radial direction to increase the wetting area. **d**, A cell suspension containing corneal cells (green) is dispensed at the bottom of the concave well, which is subsequently inverted and positioned over the dome scaffold to bring the solution in contact with the convex surface of the scaffold. Once contact is established, the device assembly is kept in a humidified cell culture incubator to allow the seeded corneal epithelial cells to adhere to the surface of the scaffold. **e**, After cell attachment, the same procedure is performed using a solution containing conjunctival epithelial cells (red). In this process, the distance between the concave well and the scaffold is reduced to spread a suspension over the entire scaffold surface and to deposit the conjunctival cells on the peripheral region of the scaffold.

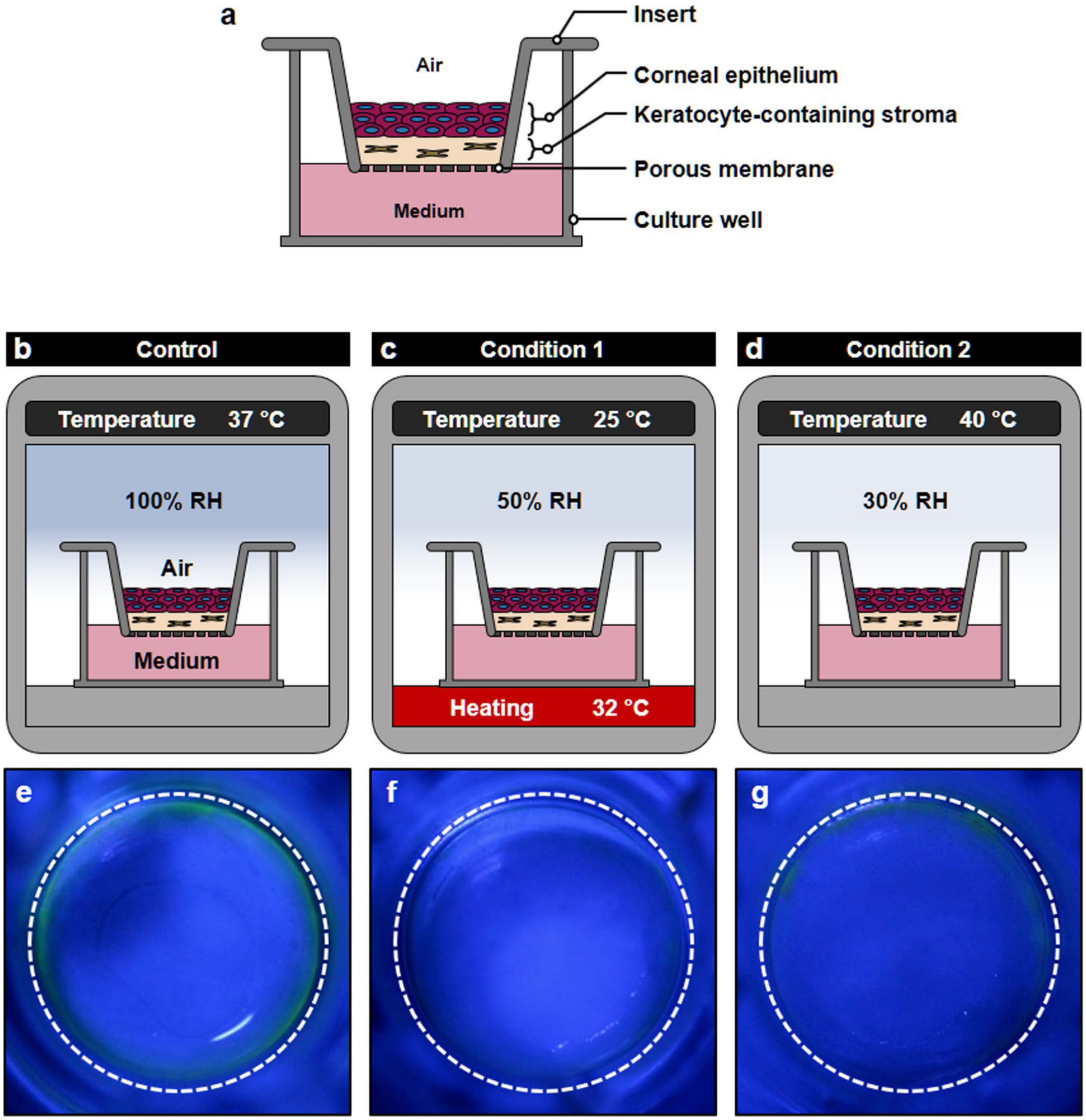

Extended Data Fig. 2 |. Responses of transwell dry-eye model to desiccating stress.

The capacity of conventional in vitro platforms to model dry eye was investigated using air-liquid interface (ALI) culture of primary human corneal epithelial cells and keratocytes in Transwell inserts. **a**, This in vitro model was constructed as a Transwell equivalent of the eye model by creating a thin layer of collagen hydrogel interspersed with keratocytes on the porous membrane of the insert and then plating corneal epithelial cells on the surface of the hydrogel layer. Before induction of dry eye, the tissue construct was cultured submerged for 3 d and then maintained at the ALI for another 10 d to induce differentiation and stratification of the epithelium. **b**–**d**, Simulation of evaporative dry eye in the Transwell model. **b**, (Control) The tissue was maintained in a regular humidified cell culture incubator (37 °C air, 100% RH). **c**, (Condition 1) The tissue constructs were moved to the DED simulation chamber to expose them under the same condition used for modeling dry eye in the eye model (25 °C air, 32 °C for culture medium and 50% RH). **d**, (Condition 2) Desiccating culture conditions previously reported in Transwell-based in vitro models of evaporative dry eye (40 °C air, 30% RH) were used. **e**–**g**, Evaluation of the response of the Transwell dry-eye models to the desiccating environment using fluorescein staining after 4 d exposure. In the Control group (**e**), no fluorescence was detected in the central regions of the epithelium when treated with fluorescein. Similarly, the ocular surface tissues produced in Conditions 1 (**f**) and 2 (**g**) showed the absence of fluorescein staining despite their exposure to the desiccating environment. RH, relative humidity.

Supplementary Material

Refer to Web version on PubMed Central for supplementary material.

Acknowledgements

We thank G. Al, R. Dana and P. Argüeso for their input to this study; I. Gipson at the Schepens Eye Research Institute for providing immortalized human conjunctival epithelial cells; G. Jay at Brown University for providing human lubricin; K. Kwon for providing data on the kinematics of blinking in the human eye; D. Song, J. Vance, D. Caggiano, M. Henderson and J. DuPont for assistance in OCT, TearLab and keratography; L. Du and M. Allen for assistance in mechanical testing; and P. McClanahan for assistance in fluorescence imaging of tear fluids. This work was supported by the National Institutes of Health (NIH) grant nos. 1DP2HL127720-01 (to D.H.), R01EY026972 (to V.Y.B.) and K08EY025742-01 (to V.L.), the National Science Foundation grant no. CMMI:15-48571 (to V.B.S. and D.H.), the Research to Prevent Blindness (to V.Y.B.) and the University of Pennsylvania. D.H. is a recipient of the NIH Director's New Innovator Award and the Cancer Research Institute Technology Impact Award.

References

1. Proksch E, Brandner JM & Jensen J-M The skin: an indispensable barrier. Exp. Dermatol 17, 1063–1072 (2008). [PubMed: 19043850]
2. Wanner A, Salathé M & O'Riordan TG Mucociliary clearance in the airways. Am. J. Respir. Crit. Care Med 154, 1868–1902 (1996). [PubMed: 8970383]
3. Turner JR Intestinal mucosal barrier function in health and disease. Nat. Rev. Immunol. 9, 799 (2009). [PubMed: 19855405]
4. Marchiando AM, Graham WV & Turner JR Epithelial barriers in homeostasis and disease. Annu. Rev. Pathol 5, 119–144 (2010). [PubMed: 20078218]
5. Gipson IK The ocular surface: the challenge to enable and protect vision: the Friedenwald lecture. Invest. Ophthalmol. Vis. Sci 48, 4391–4398 (2007).
6. Ehlers N et al. Morphological evaluation of normal human corneal epithelium. Acta Ophthalmol. 88, 858–861 (2010). [PubMed: 21114634]
7. Pfister RR & Burstein NL The normal and abnormal human corneal epithelial surface: a scanning electron microscope study. Invest. Ophthalmol. Vis. Sci 16, 614–622 (1977). [PubMed: 873722]
8. Nichols B, Dawson CR & Togni B Surface features of the conjunctiva and cornea. Invest. Ophthalmol. Vis. Sci. 24, 570–576 (1983). [PubMed: 6841003]
9. Gipson IK Distribution of mucins at the ocular surface. Exp. Eye Res 78, 379–388 (2004). [PubMed: 15106916]
10. Bron AJ et al. TFOS DEWS II pathophysiology report. Ocul. Surf 15, 438–510 (2017). [PubMed: 28736340]

11. Meloni M, De Servi B, Marasco D & Del Prete S Molecular mechanism of ocular surface damage: application to an in vitro dry eye model on human corneal epithelium. Mol. Vis 17, 113–126 (2011). [PubMed: 21245952]
12. Lu Q, Yin H, Grant MP & Elisseeff JH An in vitro model for the ocular surface and tear film system. Sci. Rep. 7, 6163–6163 (2017). [PubMed: 28733649]
13. Kwon KA et al. High-speed camera characterization of voluntary eye blinking kinematics. J. R. Soc. Interface 10, 20130227 (2013). [PubMed: 23760297]
14. Farris RL, Stuchell RN & Mandel ID Basal and reflex human tear analysis: I. Physical measurements: osmolarity, basal volumes, and reflex flow rate. Ophthalmology 88, 852–857 (1981). [PubMed: 7322504]
15. Doane MG Interaction of eyelids and tears in corneal wetting and the dynamics of the normal human eyeblink. Am. J. Ophthalmol 89, 507–516 (1980). [PubMed: 7369314]
16. Jones MB, Fulford GR, Please CP, McElwain DLS & Collins MJ Elastohydrodynamics of the eyelid wiper. Bull. Math. Biol 70, 323–343 (2008). [PubMed: 18066629]
17. Masterton S & Ahearne M Mechanobiology of the corneal epithelium. Exp. Eye Res 177, 122–129 (2018). [PubMed: 30086260]
18. Sakai E, Shiraishi A, Yamaguchi M, Ohta K & Ohashi Y Blepharo-tensiometer: new eyelid pressure measurement system using tactile pressure sensor. Eye Contact Lens 38, 326–330 (2012). [PubMed: 22890227]
19. Yamamoto Y et al. Involvement of eyelid pressure in lid-wiper epitheliopathy. Curr. Eye Res 41, 171–178 (2016). [PubMed: 25803436]
20. Shaw AJ, Collins MJ, Davis BA & Carney LG Eyelid pressure and contact with the ocular surface. Invest. Ophthalmol. Vis. Sci 51, 1911–1917 (2010). [PubMed: 19834035]
21. Shaw AJB. Eyelid Pressure on the Cornea. PhD thesis (Queensland Univ. of Technology; 2009).
22. Molladavoodi S, Robichaud M, Wulff D & Gorbet M Corneal epithelial cells exposed to shear stress show altered cytoskeleton and migratory behaviour. PloS ONE 12, e0178981 (2017). [PubMed: 28662184]
23. Ren H & Wilson G The effect of a shear force on the cell shedding rate of the corneal epithelium. Acta Ophthalmol. Scand. 75, 383–387 (1997). [PubMed: 9374244]
24. Nowell CS & Radtke F Corneal epithelial stem cells and their niche at a glance. J. Cell Sci. 130, 1021–1025 (2017). [PubMed: 28202689]
25. Tsubota K Tear dynamics and dry eye. Prog. Retin. Eye Res 17, 565–596 (1998). [PubMed: 9777650]
26. Willcox MDP et al. TFOS DEWS II tear film report. Ocul. Surf 15, 366–403 (2017). [PubMed: 28736338]
27. Bunya VY et al. Variability of tear osmolarity in patients with dry eye. JAMA Ophthalmol. 133, 662–667 (2015). [PubMed: 25811641]
28. Stevenson W, Chauhan SK & Dana R Dry eye disease: an immune-mediated ocular surface disorder. Arch. Ophthalmol 130, 90–100 (2012). [PubMed: 22232476]
29. Rhee MK & Mah FS Inflammation in dry eye disease: how do we break the cycle? Ophthalmology 124, S14–S19 (2017). [PubMed: 29055357]
30. Schlote T, Kadner G & Freudenthaler N Marked reduction and distinct patterns of eye blinking in patients with moderately dry eyes during video display terminal use. Graefe’s Arch. Clin. Exp. Ophthalmol. 242, 306–312 (2004). [PubMed: 14747951]
31. Abdelfattah NS, Dastiridou A, Sadda SR & Lee OL Noninvasive imaging of tear film dynamics in eyes with ocular surface disease. Cornea 34, S48–S52 (2015). [PubMed: 26226477]
32. Tian L, Qu JH, Zhang XY & Sun XG Repeatability and reproducibility of noninvasive keratograph 5M measurements in patients with dry eye disease. Am. J. Ophthalmol 2016, 8013621 (2016).
33. Koh S et al. Regional differences in tear film stability and meibomian glands in patients with aqueous-deficient dry eye. Eye Contact Lens 42, 250–255 (2016). [PubMed: 26383772]
34. Bron AJ, Argueso P, Irkec M & Bright FV Clinical staining of the ocular surface: mechanisms and interpretations. Prog. Retin. Eye Res 44, 36–61 (2015). [PubMed: 25461622]

35. Jay GD & Waller KA The biology of lubricin: near frictionless joint motion. Matrix Biol. 39, 17–24 (2014). [PubMed: 25172828]
36. Jay GD Lubricin and surfacing of articular joints. Curr. Opin. Orthop 15, 355–359 (2004).
37. Schmidt TA, Sullivan DA & Knop E et al. Transcription, translation, and function of lubricin, a boundary lubricant, at the ocular surface. JAMA Ophthalmol. 131, 766–776 (2013). [PubMed: 23599181]
38. Samsom ML et al. Characterization of full-length recombinant human Proteoglycan 4 as an ocular surface boundary lubricant. Exp. Eye Res. 127, 14–19 (2014). [PubMed: 24997456]
39. Regmi SC et al. Degradation of proteoglycan 4/lubricin by cathepsin S: potential mechanism for diminished ocular surface lubrication in Sjögren's syndrome. Exp. Eye Res. 161, 1–9 (2017). [PubMed: 28549901]
40. Lambiase A et al. A two-week, randomized, double-masked study to evaluate safety and efficacy of lubricin (150 μg/mL) eye drops versus sodium hyaluronate (HA) 0.18% eye drops (Vismed®) in patients with moderate dry eye disease. Ocul. Surf 15, 77–87 (2017). [PubMed: 27614318]
41. Lee HS et al. Expression of toll-like receptor 4 contributes to corneal inflammation in experimental dry eye disease. Invest. Ophthalmol. Vis. Sci 53, 5632–5640 (2012). [PubMed: 22789921]
42. Verstrepen L et al. TLR-4, IL-1R and TNF-R signaling to NF-κB: variations on a common theme. Cell. Mol. Life Sci. 65, 2964–2978 (2008). [PubMed: 18535784]
43. Pitenis AA et al. Friction-induced inflammation. Tribology Lett. 66, 81 (2018).
44. Pitenis AA et al. Corneal cell friction: survival, lubricity, tear films, and mucin production over extended duration in vitro studies. Biotribology 11, 77–83 (2017).
45. Chao W et al. Report of the inaugural meeting of the TFOS i(2) = initiating innovation series: targeting the unmet need for dry eye treatment. Ocul. Surf 14, 264–316 (2016). [PubMed: 26774910]
46. Baudouin C et al. Clinical impact of inflammation in dry eye disease: proceedings of the ODISSEY group meeting. Acta Ophthalmol. 96, 111–119 (2018). [PubMed: 28390092]
47. Hall A The origin and purposes of blinking. Br. J. Ophthalmol. 29, 445–467 (1945). [PubMed: 18170143]
48. Warren HS et al. Mice are not men. Proc. Natl Acad. Sci. USA 112, E345 (2015). [PubMed: 25540422]
49. Al-Sharif A et al. Lubricin/Proteoglycan 4 binding to CD44 receptor: a mechanism of the suppression of proinflammatory cytokine-induced synoviocyte proliferation by lubricin. Arthritis Rheumatol. 67, 1503–1513 (2015). [PubMed: 25708025]
50. Iqbal SM et al. Lubricin/Proteoglycan 4 binds to and regulates the activity of toll-like receptors. Vitr. Sci. Rep. 6, 18910 (2016).
51. Waller KA, Zhang LX & Jay GD Friction-induced mitochondrial dysregulation contributes to joint deterioration in prg4 knockout mice. Int. J. Mol. Sci 18, 1252 (2017).
52. Shaheen B, Bakir M & Jain S Corneal nerves in health and disease. Surv. Ophthalmol. 59, 263–285 (2014). [PubMed: 24461367]
53. Belmonte C et al. TFOS DEWS II pain and sensation report. Ocul. Surf. 15, 404–437 (2017). [PubMed: 28736339]
54. Dartt DA Neural regulation of lacrimal gland secretory processes: relevance in dry eye diseases. Prog. Retin. Eye Res 28, 155–177 (2009). [PubMed: 19376264]

References

55. Morrison S, Sullivan DA, Sullivan BD, Sheardown H & Schmidt TA Dose-dependent and synergistic effects of proteoglycan 4 on boundary lubrication at a human cornea-polydimethylsiloxane biointerface. Eye Contact Lens 38, 27–35 (2012). [PubMed: 22157393]
56. Jay GD, Tantravahi U, Britt DE, Barrach HJ & Cha CJ Homology of lubricin and superficial zone protein (SZP): products of megakaryocyte stimulating factor (MSF) gene expression by human synovial fibroblasts and articular chondrocytes localized to chromosome 1q25. J. Orthop. Res. 19, 677–687 (2001). [PubMed: 11518279]

57. Schiffman RM, Christianson MD, Jacobsen G, Hirsch JD & Reis BL Reliability and validity of the Ocular Surface Disease Index. Arch. Ophthalmol 118, 615–621 (2000). [PubMed: 10815152]

58. Bunya VY et al. Development and evaluation of semiautomated quantification of lissamine green staining of the bulbar conjunctiva from digital images. JAMA Ophthalmol. 135, 1078–1085 (2017). [PubMed: 28910455]

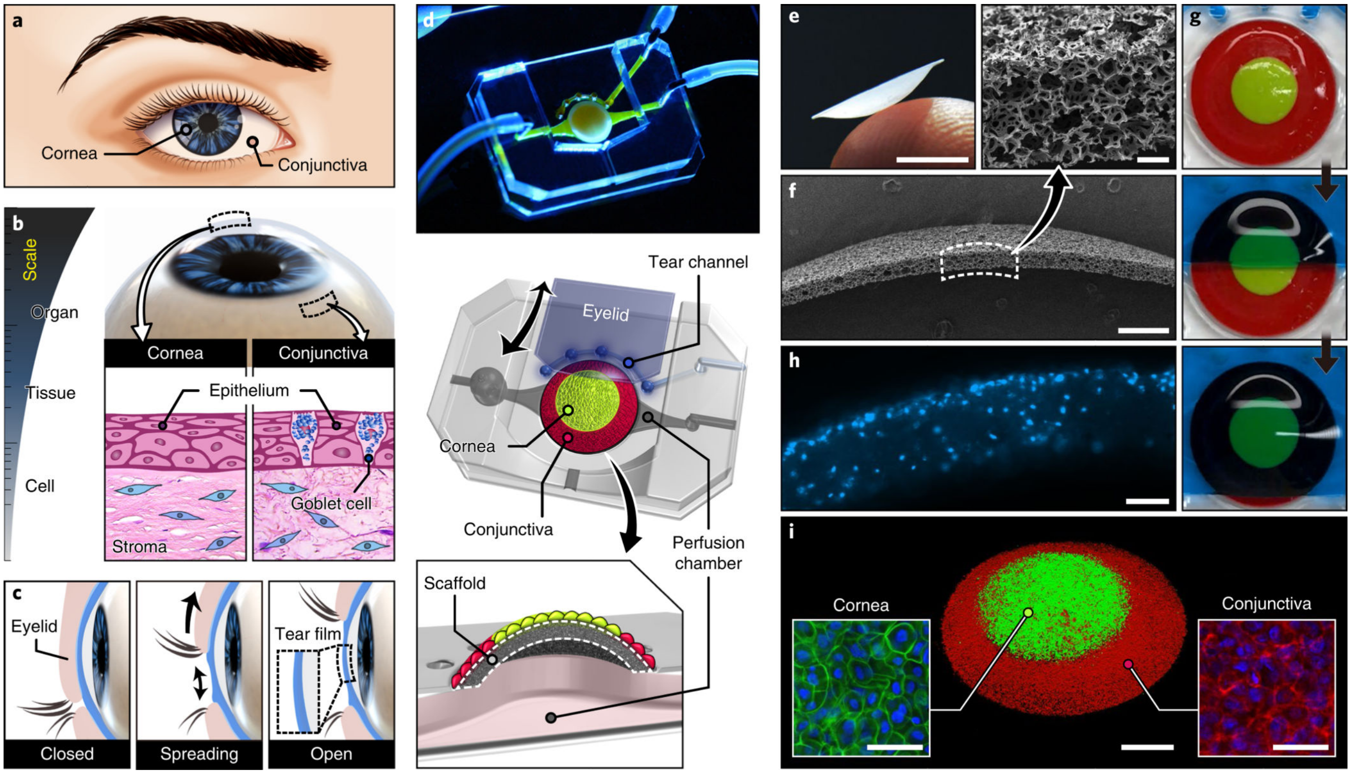

Fig. 1 |. A reverse engineered human ocular surface.

a, The cornea and conjunctiva together form the ocular surface. **b**, The 3D dome-shaped ocular surface at the organ scale consists of multilayered tissue structures assembled by different types of cells. **c**, Formation of a thin tear film on the ocular surface during spontaneous eye blinking. **d**, Photograph and schematic illustration of a multilayered elastomeric device used to emulate the human ocular surface. **e**, Photograph of a thin-walled dome scaffold on the tip of a human finger. Scale bar, 3 mm. **f**, Scanning electron micrographs of the scaffold. Scale bars, 500 μm (lower micrograph) and 50 μm (upper inset). **g**, Sequential images of a hydrogel eyelid sliding over the engineered ocular surface. For visualization, the corneal and conjunctival regions of the scaffold were dyed with green- and red-colored PDMS, respectively. **h**, Cross-sectional image of the scaffold seeded with primary human keratocytes in an extracellular matrix hydrogel. Blue, DAPI. Scale bar, 100 μm. **i**, 3D rendered confocal micrograph of human corneal (stained with CellTracker Green) and conjunctival (stained with CellTracker Red) epithelial cells on the surface of the scaffold. Scale bars, 1 mm (middle) and 50 μm (insets). This experiment was replicated three times.

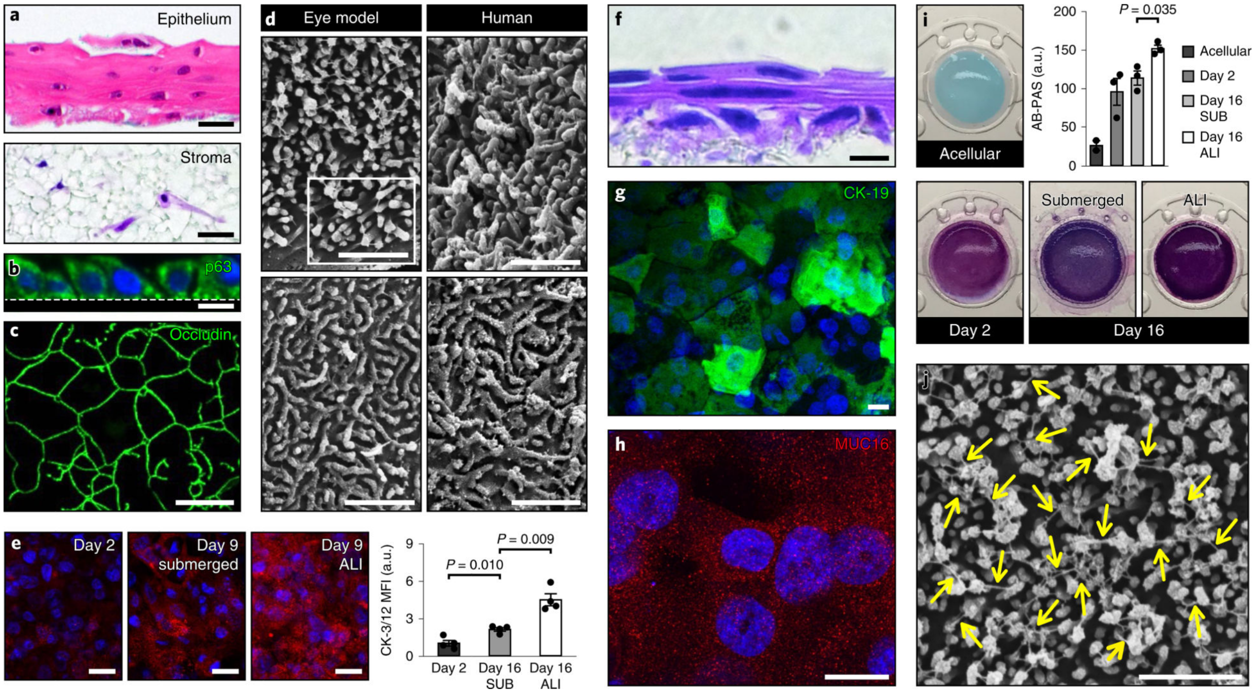

Fig. 2 |. Tissue engineering of the human cornea and conjunctiva in the biomimetic eye model.

a, Representative H&E images of the stratified corneal epithelium (top) and the keratocyte-laden stroma (bottom). Scale bars, 20 µm. This experiment was replicated three times. **b**, Immunofluorescence staining of p63 in the stratified corneal epithelial cells. The dotted line indicates the boundary between the epithelium and the stroma. Green, p63; blue, DAPI. Scale bar, 15 µm. This experiment was replicated twice. **c**, Representative image of occludin in the differentiated corneal epithelium. The cells were imaged by immunofluorescence staining in three independent experiments. Green, occludin. Scale bar, 100 µm. **d**, Scanning electron micrographs of microvilli (top row) and microplicae (bottom row) on the surface of the differentiated corneal epithelium in our model (left column) and in the human eye (right column). Scale bar, 1 µm. Images were obtained from three engineered eye devices and two human cornea samples. **e**, Immunofluorescence images of CK-3/12 expression in the corneal epithelial cells. SUB represents the submerged group. ALI was initiated on day 2. Images were acquired from four independent experiments. Red, CK-3/12; blue, DAPI. Scale bar, 20 µm. Quantified data show mean fluorescence intensity (MFI) normalized to the day 2 group. Error bars indicate s.e.m. *P* values by unpaired, two-sided *t*-test. **f**, Representative H&E image of the stratified conjunctival epithelial cells. This experiment was replicated three times. Scale bar, 20 µm. **g**,**h**, Immunofluorescence micrographs of CK-19 (**g**) and MUC16 (**h**) expressed by the conjunctival epithelial cells. Green, CK-19; red, MUC16; blue, DAPI. Scale bars, 20 µm. The images are representatives of two independent experiments. **i**, Representative images from AB-PAS staining of the engineered ocular surface. ALI was initiated on day 2. SUB represents the submerged group. Data represent mean ± s.e.m. of staining intensity normalized to the Acellular group from three independent experiments. *P* values by unpaired, two-sided *t*-test. **j**, Scanning electron micrograph showing a network of nanofilaments (shown with yellow arrows) on the engineered ocular surface. Scale bar, 1 µm. This experiment was replicated three times. a.u., arbitrary unit.

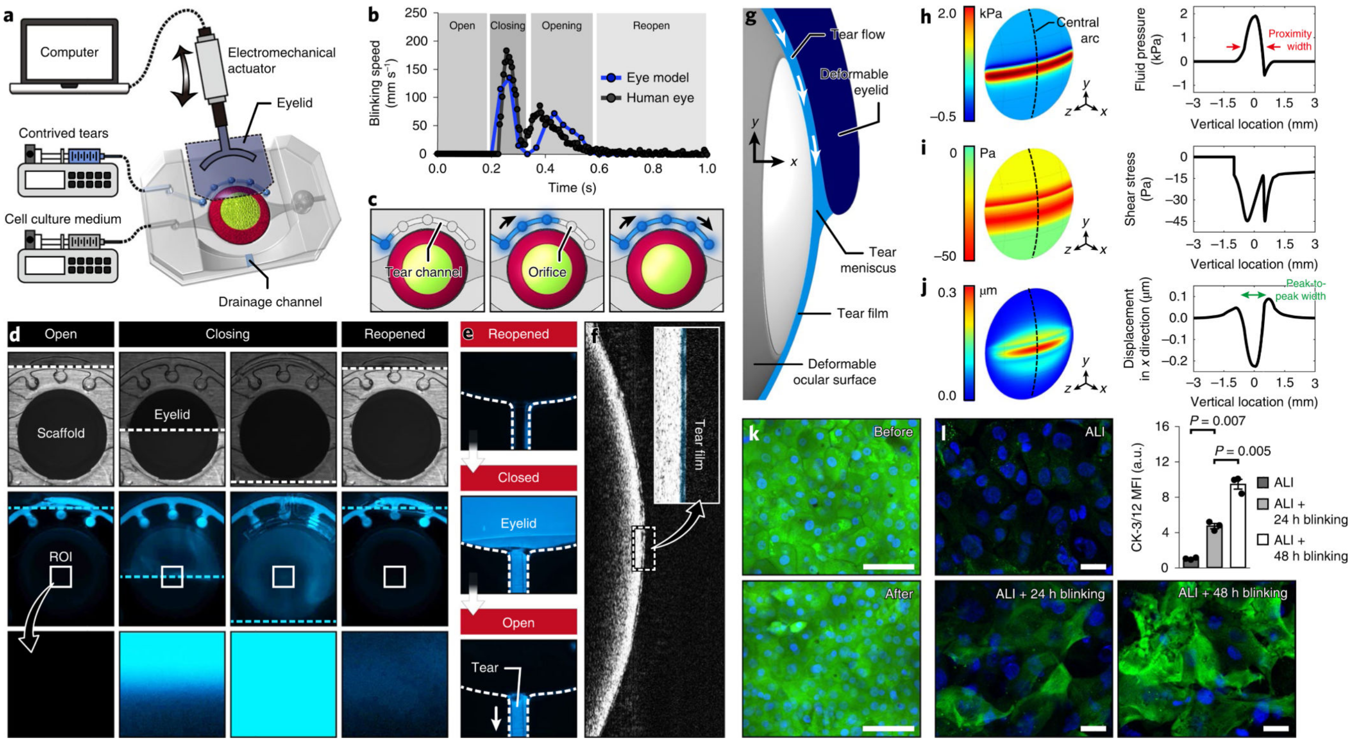

Fig. 3 |. Recapitulation of eye blinking and physiological biomechanical environment of the ocular surface.

a, Schematic of the experimental setup to simulate eye blinking that uses a computer-controlled electromechanical actuator to induce back-and-forth motion of the biomimetic eyelid. **b**, Kinematics of spontaneous blinking in the human eye (gray) and hydrogel eyelid actuation in our device (blue). Analysis of blinking speed in our system was performed twice. The human data were provided by Dr. Kyung-Ah Kwon at the University of Cambridge. **c**, Sequential illustration of tear injection and flow in the tear channel. **d**, Bright field (top row) and fluorescence (middle and bottom rows) images showing sequential phases of blinking and corresponding distribution of fluorescently labeled tear fluid (blue). The bottom row shows a blow-up of the region of interest (ROI) at the center of the ocular surface. The dotted lines in the top and middle rows indicate the eyelid margin. This experiment was replicated three times. **e**, Sequential fluorescence images showing the clearance of excess tear fluid pushed by the eyelid into the drainage channel during blinking. The dotted lines show the channel walls. This experiment was replicated three times. **f**, OCT images of a thin tear film on the ocular surface. The tear film is pseudo-colored blue in the inset. This experiment was replicated twice. **g**, Schematic of the elasto-hydrodynamic model of our in vitro system that includes blink-induced flow in the tear film and the deformation of the engineered ocular surface and the moving eyelid. The margin of the eyelid is located 1 mm below the mid-line during the down phase of a blink. **h**, Distribution of tear fluid pressure in the engineered ocular surface predicted by the theoretical model. The arrows in the graph mark the width of the proximity region in which pressure is positive and higher than 0.6 kPa. **i**,**j**, Heat maps of fluid shear stress (**i**) and the vertical displacement of the engineered ocular surface (**j**). The peak-to-peak width in **j** represents the width of depression. **k**, Viability staining of the epithelial cells before and after 150 cycles of blinking. Green, calcein AM; blue, DAPI. Scale bar, 100 µm. This experiment was replicated three times. **l**, Immunofluorescence images of CK-3/12 (green) in the corneal epithelial cells. Top left, 2 d submerged culture followed by 3 d ALI culture without blinking. Bottom left, 2 d submerged culture followed by 2 d ALI culture without blinking and an additional 1 d ALI culture with blinking. Bottom right, 2 d submerged culture followed by 1 d ALI culture without blinking and an additional 2 d ALI culture with blinking. Green, CK-3/12; blue, DAPI. Scale bar, 20 µm. Data are mean ± s.e.m. of fluorescence intensity normalized to the ALI group from three independent experiments. *P* values by unpaired, two-sided *t*-test.

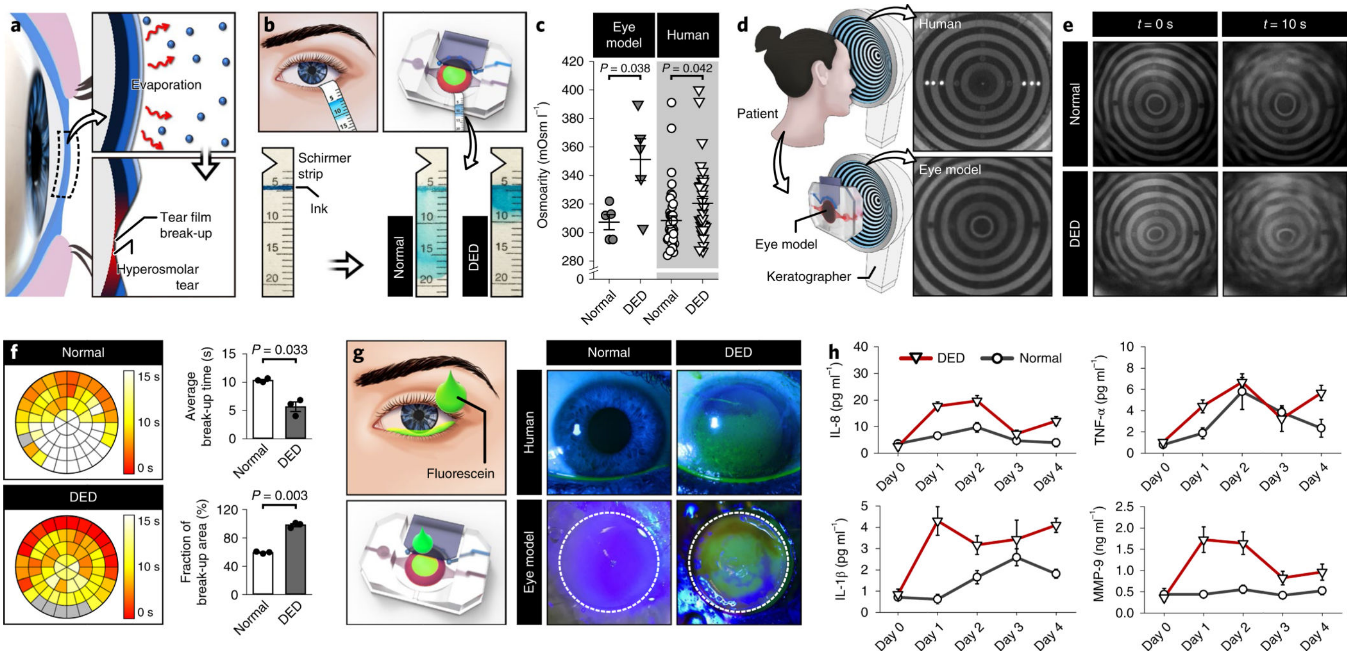

Fig. 4 |. An engineered model of evaporative dry eye.

a, Abnormal loss of water from the tear film due to evaporation causes the break-up of the tear film and increased tear osmolarity that together lead to a loss of homeostasis. **b**, Absorption of tears into the Schirmer strips in the normal and dry-eye models. Tear absorption is visualized by the smearing of the blue ink within the strips. **c**, Tear osmolarity in the DED (closed triangle) and the normal (closed circle) models. Data were obtained from five independent experiments. Human clinical data of osmolarity are repeated measurements from 9 normal subjects (open circle) and 12 patients with DED (open triangle). Data show mean ± s.e.m. **d**, Keratographs showing concentric rings projected on the human ocular surface (top) and on the engineered ocular surface (bottom). The images are representatives from three independent experiments. **e**, Representative images of projected ring patterns on the engineered ocular surface of the normal (top row) and the DED (bottom row) groups captured at $t = 0$ s (left column) and $t = 10$ s (right column). This experiment was replicated three times. **f**, Spatial mapping of tear film break-up time in the normal (top) and the DED (bottom) models. Different colors in the representative circular heat maps indicate different tear break-up times. Quantified data in the graphs are mean ± s.e.m. of average tear film break-up time and area from three independent experiments. *P* values by unpaired, two-sided *t*-test. **g**, Fluorescein staining of the eye model and human subjects. The representative images of the eye model are from three independent experiments. The dotted lines show the outline of the scaffold. **h**, Concentrations of inflammatory mediators (IL-8, TNF-α, IL-1β and MMP-9) in the normal (circle) and the DED (triangle) groups plotted against the duration of culture. In the DED group, disease induction began on day 0. Data represent mean ± s.e.m. from three independent experiments. See source data for statistical analysis.

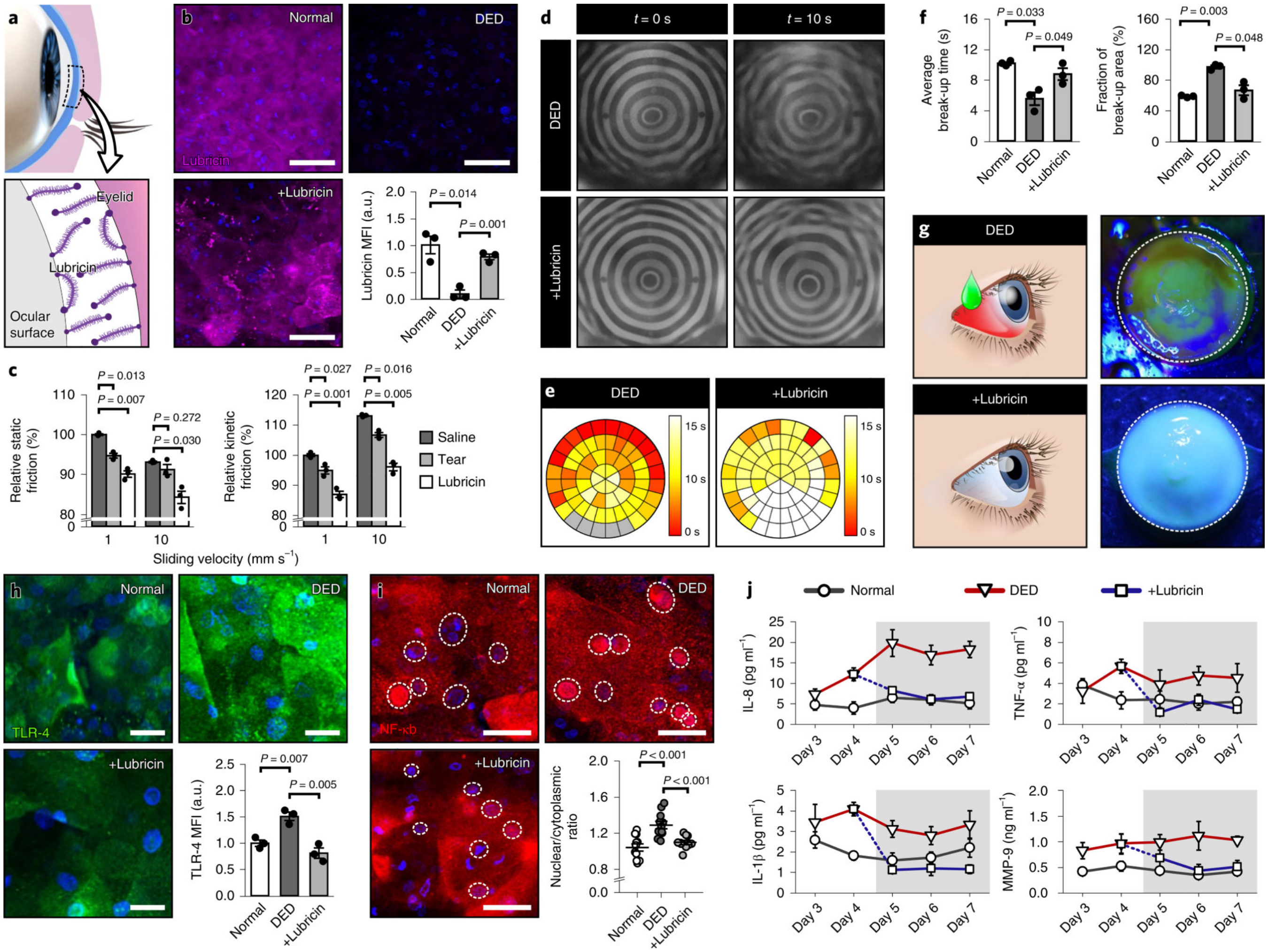

Fig. 5 |. Evaluation of therapeutic efficacy of lubricin.

a, Lubricin adheres to the corneal and conjunctival epithelia and acts to lubricate the interface between the ocular surface and the eyelid. **b**, Immunofluorescence images of lubricin in the corneal epithelial cells in the normal, DED and lubricin-treated DED (+Lubricin) models. In the +Lubricin group, the engineered tissue was topically treated with human lubricin for 3 d. Representative fluorescence images of cells and quantified results are from three independent experiments. Magenta, lubricin; blue, DAPI. Scale bar, 50 μm. Data are mean ± s.e.m. of fluorescence intensity normalized to the normal group. *P* values by unpaired, two-sided *t*-test. **c**, Static and kinetic friction between the engineered ocular surface and the hydrogel eyelid. Saline, contrived tears and lubricin were used as lubricants. Friction is shown as a percentage relative to the saline control. Data show mean ± s.e.m, and *P* values are from unpaired, two-sided *t*-test. **d**, Representative keratographs of the DED (top row) and lubricin-treated DED (+Lubricin; bottom row) from three independent experiments. The keratographs in Fig. 4e were repeated in the top row for comparison purposes. **e**,**f**, Heat maps of tear film break-up time (**e**) and quantification of average tear break-up time and area (**f**). The circular map for the +Lubricin group in **e** is representative of three independent experiments, and color-coding indicates different tear break-up times.

Quantified results in **f** show mean ± s.e.m., and *P* values are from unpaired, two-sided *t*-test. For comparison, the data presented in Fig. 4f were reused in **e** and **f** to represent the normal and DED groups. **g**, Fluorescein staining of the engineered ocular surface in the +Lubricin group (bottom row) after 3 d lubricin treatment. The image is representative of three independent experiments. The image for the DED model (top row) was borrowed from Fig. 4g. **h**, Immunofluorescence staining of TLR-4 on the corneal epithelium in the normal, DED and lubricin-treated models. Green, TLR-4; blue, DAPI. Scale bar, 50 μm. Quantified data show mean ± s.e.m. of fluorescence intensity normalized to the normal group. *P* values by unpaired, two-sided *t*-test. **i**, Immunofluorescence images of NF-κB in the corneal epithelial cells. Cell nuclei are outlined with dotted circles. Red, NF-κB; blue, DAPI. Scale bar, 50 μm. NF-κB translocation in the scatter plot was quantified by calculating the ratio of nuclear to cytoplasmic red fluorescence intensity. Data are mean ± s.e.m. from three independent experiments. *P* values by unpaired, two-sided *t*-test. **j**, Production of pro-inflammatory mediators (IL-8, TNF-α, IL-1β and MMP-9) in the normal (circle), DED (triangle) and the lubricin-treated (square) groups. Shaded regions in the graphs indicate the period of drug treatment. The data points for days 3 and 4 were borrowed from Fig. 4h to show the trends more clearly. See source data for statistical analysis.